Research article

Heiko Kollmann, Martin Esmann, Julia Witt, Aleksandra Markovic, Vladimir Smirnov, Gunther Wittstock, Martin Silies* and Christoph Lienau

Fourier-transform spatial modulation spectroscopy of single gold nanorods

https://doi.org/10.1515/nanoph-2017-0096
Received September 27, 2017; revised November 21, 2017; accepted November 30, 2017

Abstract: Sensing the scattered fields of single metallic nanostructures is a crucial step towards the applications of isolated plasmonic antennas, such as for the sensing of single molecules or nanoparticles. In the past, both near- and far-field spectroscopy methods have been applied to monitor single plasmonic resonances. So far, however, these spectral-domain techniques do not yet provide the femtosecond time resolution that is needed to probe the dynamics of plasmonic fields in the time domain. Here, we introduce a time-domain technique that combines broadband Fourier-transform spectroscopy and spatial modulation spectroscopy (FT-SMS) to quantitatively measure the extinction spectra of the isolated gold nanorods with a nominal footprint of 41×10 nm^2. Using a phase-stable pulse pair for excitation, the technique is capable of rejecting off-resonant stray fields and providing absolute measurements of the extinction cross section. Our results indicate that the method is well suited for measuring the optical response of strongly coupled hybrid systems with high signal-to-noise ratio. It may form the basis for new approaches towards time-domain spectroscopy of single nanoantennas with few-cycle time resolution.

Keywords: spatial modulation spectroscopy; Fourier-transform spectroscopy; localized surface plasmon resonance; gold nanorods; field autocorrelation; extinction cross section.

***Corresponding author: Martin Silies,** Institute of Physics and Center of Interface Science, Carl von Ossietzky University, 26111 Oldenburg, Germany, e-mail: martin.silies@uni-oldenburg.de. http://orcid.org/0000-0002-3704-2066
Heiko Kollmann, Martin Esmann, Vladimir Smirnov and Christoph Lienau: Institute of Physics and Center of Interface Science, Carl von Ossietzky University, Oldenburg, Germany
Julia Witt, Aleksandra Markovic and Gunther Wittstock: Institute of Chemistry and Center of Interface Science, Carl von Ossietzky University, Oldenburg, Germany

1 Introduction

Plasmonic nanoantennas, such as gold nanorods, have attracted much research interest in the last decades due to their ability to confine and enhance optical fields on nanometer scales. Their strongly localized surface plasmon (SP) resonance enhances the electric field in the vicinity of the nanoantenna [1–3]. This resonance can be tuned from the visible to near-infrared spectral range by varying the overall size or aspect-ratio of the nanorod [4–7]. In addition, the strong optical near-fields of such nanorods may enable enhanced coupling to other metal nanostructures [8] and to resonantly-matched excitonic quantum emitters [9]. This has recently led to a series of optical studies of metal/quantum emitter nanostructures, motivated for instance by interest in the fundamental optical properties and possible practical applications, such as in integrated optics, optoelectronics [10, 11] or molecular sensing [12], of such hybrid structures [13]. While the linear optical spectra of the selected hybrid exciton/plasmon systems have been studied in some detail [9, 14–19] the time-resolved studies of the coherent energy transfer processes [20, 21] in the single hybrid nanostructures are still lacking. Such experiments would require probing the transient electric fields emitted by the nanorods with high time resolution in the range of 10 fs or even below, which are limited by the comparatively short dephasing times of single plasmonic nanostructures. Furthermore, they must be sufficiently sensitive to probe the small extinction cross sections of single metallic nanoparticles of typically just a few hundreds or thousands of nm^2.

So far, the optical response of the single metallic nanoparticles has mainly been studied by far-field spectroscopy methods, such as dark-field microscopy [22–25], photo-thermal [26–28] and total internal reflection imaging [29]. Dark-field and total internal reflection microscopy, as a relatively simple platform, provides spectral information about the scattering properties of the particle, but are typically limited to particle dimensions

of about 20 nm [30, 31]. The photothermal imaging microscopy, in contrast, measures the absorption properties and is capable of detecting particles as small as a few nanometers [32]. Spatial modulation spectroscopy (SMS) was introduced as a far-field confocal microscopy technique to provide quantitative, spectrally-resolved information about the extinction cross section, i.e. the sum of absorption and scattering cross section of the nanoparticles [33–38]. In SMS, the position of a confocal light spot is periodically modulated with respect to the position of the nanoparticle or vice-versa while simultaneously detecting the transmitted light using a combination of a photodetector and a lock-in amplifier. This technique has successfully been applied to determine the absolute extinction cross section of single gold nanoparticles with diameters down to 5 nm [33, 39, 40]. First experiments in this direction were performed using the monochromatic light sources for excitation of the nanoparticle [33, 38]. Given that the light is typically detected using a fast photodetector, spectral information is obtained by scanning the excitation wavelength [36, 41, 42]. The quantitative measures of the absorption [43] and extinction [40, 44] cross section of single plasmonic structures can also obtained using photothermal imaging and dark-field microscopy, respectively. Probing the dynamics of intrinsically short-lived coherent plasmonic fields in the time domain is difficult when using existing techniques, because they are mostly based on spectrally narrow excitation sources or dispersive glass objectives. In contrast, the dispersion-free set-up described here has the potential of measuring electric fields emitted from single nanoparticles in the time-domain in a nearly dispersion-free set-up, which can be easily upgraded towards a pump-probe experiment to allow time-domain studies on a femtosecond time scale. Such time-domain studies would not only allow probing transient field dynamics but also the study of the coherent energy transfer processes in the hybrid systems. For this, it seems interesting to explore time-domain methods for measuring single particle extinction. Furthermore, it may be interesting that the two-dimensional electronic spectroscopy of single plasmonic nanoparticles is almost realized. Such experiments can give important insights into the energy and charge transfers processes on the nanoscale and are of interest for probing the rich physics of plasmonic nanostructures, which are coupled to single or ensembles of quantum emitters.

In this work, we report on a coherent, time-domain spectroscopy method to measure the absolute extinction cross section and the power spectrum of the single gold nanorods by a combination of coherent Fourier-transform spectroscopy and spatial modulation spectroscopy (FT-SMS). This technique is based on using a pair of phase-locked pulses from a dispersion-balanced Mach-Zehnder interferometer to excite the localized plasmon resonance in a single gold nanorod. Our analysis shows that this combination of coherent FTS and SMS provides a quantitative measurement of the extinction cross section and can separate fields from the plasmonic nanoparticle and non-resonant background fields. The extension of this collinear phase-locked excitation scheme may open up the possibility of mapping and manipulating the time evolution of transient electric fields and, hence, probe ultrafast energy transfer from excitonic to plasmonic systems in the time domain [45–47].

2 Results and discussion

We developed the set-up depicted in Figure 1A to sensitively measure the extinction spectra of the isolated gold nanorods. A supercontinuum laser source (SC-450-4, Fianium, UK) generates coherent ultra-broadband pulses with a time structure $E_0(t)=\frac{1}{2\pi}\int_{-\infty}^{\infty}\tilde{E}_0(\omega)e^{-i\omega t}d\omega$. Its spectral intensity distribution $I(\omega)=\frac{\varepsilon_0 c}{2}\cdot\left|\tilde{E}_0(\omega)\right|^2$ spans the visible to near-infrared spectral region from 1 to 2 eV. The complete spectral distribution $I(\omega)$ of the laser source is shown in Figure S5 under the Supporting Information section. The supercontinuum generation leads to a rather complicated spectral phase of the pulses with picosecond duration. A phase-locked pair of these pulses $\boldsymbol{E}(\mathbf{r},t)=\boldsymbol{E}_0(\mathbf{r},t)+\boldsymbol{E}_0(\mathbf{r},t+\tau)$, separated by a variable time delay τ, is then created in a dispersion-balanced Mach-Zehnder interferometer. A broadband linear polarizer and a half-wave plate are used to control the polarization state of these pulses. An all-reflective objective (ARO) O1 (5006-000, Beck Optronics Solutions, UK) with a numerical aperture $NA_{O1}=0.65$ focuses the incoming pulses onto the sample surface. The numerical aperture and the finite obscuration of the objective limits the acceptance angles from $\theta_{min}=\mathrm{asin}(0.41\cdot NA_{O1})$ to $\theta_{max}=\mathrm{asin}(NA_{O1})$. As shown in Figure 1B, the transmitted light from the sample is then collected by a second objective O2 (5002-000, Beck Optronics Solutions, UK) with a slightly lower numerical aperture $NA_{O2}=0.5$ and acceptance angles between $\Theta_{min}=\mathrm{asin}(0.44\cdot NA_{O2})$ and $\Theta_{max}=\mathrm{asin}(NA_{O2})$. The advantages of these AROs is that they can fully preserve the time structure of broadband light pulses and thus allow focusing for few-cycle optical pulses [48], whereas the conventional, high N.A. glass objectives generally limit

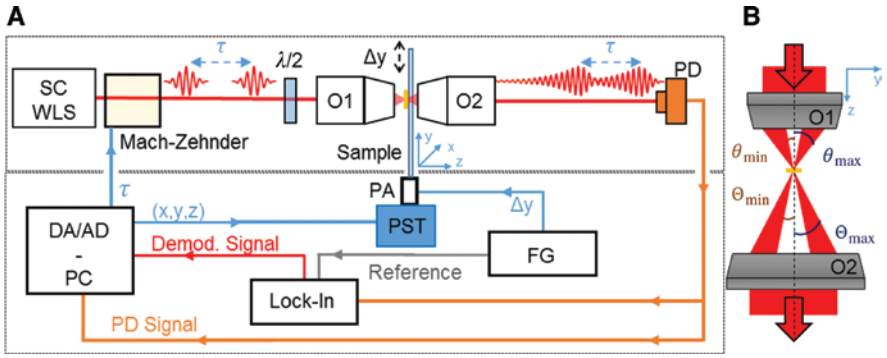

Figure 1: Schematic description of the Fourier-transform spatial modulation spectroscopy (FT-SMS) set-up.
(A) The upper box represents the optical part, and the electronic set-up is depicted in the lower part. A pair of linearly polarized, ultra-broadband laser pulses from a supercontinuum white light source (SC WLS) with adjustable time delay τ is focused to a diffraction-limited spot onto the sample using an all-reflective objective (O1). The polarization state of the incident pulse pair is controlled using an achromatic half wave plate ($\lambda/2$). The transmitted light is collected by a second all-reflective objective (O2) and focused onto a photodiode (PD). The gold nanorod sample is positioned by a PC-controlled, three-axis piezo stage (PST). A piezo actuator (PA) driven by a function generator (FG) periodically modulates the sample in the vertical, *y*-direction. The voltage from the photodiode PD and the demodulated signal from a phase-sensitive lock-in amplifier are simultaneously recorded by an analog-to-digital (AD) converter card and fed into the PC. (B) The illustration of the minimum and maximum acceptance angles of the focusing and collecting objectives.

the time resolution to more than 10 fs. A drawback is their finite N.A., which is limited to 0.65, and the finite obscuration of the ARO, resulting from the inner acceptance angle Θ_{min} and leading to a ~0% reduction in transmission in comparison to a glass objective of the same NA. The second ARO with slightly reduced NA is chosen for reasons of practical availability. The transmitted power is recorded by an amplified photodiode (PDA36A, Thorlabs, USA) and analyzed in the electronic set-up shown in the lower box of Figure 1A.

The sample position in the confocal plane of the objectives is controlled by a three-dimensional nanopositioning system (NanoCube P-611.3, Physik Instrumente, Germany). An additional periodic modulation along the vertical axis is applied through a piezo actuator (PST150/7/20VS12, Piezomechanik, Germany) by a sinusoidal driving voltage. The modulation amplitude is set to $A_m \approx 500$ nm with a modulation frequency of $f_m = 1$ kHz. The output of the photodiode is connected to a phase-sensitive lock-in amplifier (830 DSP, Stanford Research Systems, USA) and an analog-to-digital converter card (DT 9836/9818, Data Translation, USA). The signal from the output of the lock-in amplifier and the power from the photodiode are recorded while simultaneously modulating and scanning the sample position in the confocal plane. In Figure 1B, the acceptance angles of both the focusing and the collecting all-reflective objectives are illustrated. The field distribution $\mathbf{E}_F(\mathbf{r})$ in the focal plane is well described by an Airy function [49] (for details see Supporting Information, Chapter S1 and S2). The focus diameter is ~0.6 µm, corresponding to a focal area of ~0.3 µm².

The present experiments are performed at moderate power levels of ~10 µW, which is sufficiently low to suppress unwanted thermal heating of the sample. This corresponds to an average power density of 33 W/m², similar to that applied in previous frequency-domain SMS measurements [50]. Considering our pulse duration of 5 ps, this leads to a peak intensity on the sample of $1.6 \cdot 10^7$ W/cm², which is sufficiently low to avoid nonlinear processes. Rather long lock-in integration times of ~50 ms per pixel are chosen, resulting in acquisition speeds of 30–60 s per spectrum. We estimate that this speed can further by increased by 1 to 2 orders of magnitude when approaching shot-noise limited detection.

In the experiment, we measure the extinction of the single gold nanorods (E12-10-808-NPO-Hex, NanoPartz, USA) with nominal sizes, as determined by the vendor of dx = 41 nm, dy = 10 nm and dz = 10 nm. Standard deviations of the particle dimensions are $std_x = 10$ nm and $std_y = 3$ nm, as determined by SEM (see Supporting Information, Chapter S3). The nanorods are dispersed on a glass coverslip (BK-7) with a density of about 0.1 µm^{-2}. The frequency-dependent optical response of the nanorod along the long axis *x* and the short axes *y* and *z* can be well described by the polarizability tensor $\ddot{\alpha}$ of a prolate spheroid (see Supporting Information, Chapter S3). The absorption cross sections $\sigma_A(\omega)$ and the scattering cross sections $\sigma_S(\omega)$ for light that is linearly polarized along each principal axis j are hence defined by the main diagonal elements *jj* of the polarizability tensor as

$$\sigma_{A,jj}(\omega) = k \cdot \mathrm{Im}(\alpha_{jj}(\omega)), \quad (1)$$

and

$$\sigma_{S,jj}(\omega) = \frac{k^4}{6\pi}\left|\alpha_{jj}(\omega)\right|^2, \quad (2)$$

with k as the incident wave vector. For our nanorods, the fundamental longitudinal SP resonance, polarized along the long axis of the nanorod, is centered at ~1.67 ev, whereas the transverse SP resonance is at higher energy (~2.5 eV, see Supporting Information, Chapter S3) [42]. Hence, only the longitudinal SP resonance with the polarizability α_{xx} lies in the detectable spectral range of the experimental set-up. Furthermore, the expected absorption cross section $\sigma_{A,xx} = 3500$ nm^2 of the nanorods is more than a factor of 30 larger than its scattering cross section $\sigma_{S,xx} = 100$ nm^2 [51]. Hence, the extinction cross section $\sigma_{E,xx} = \sigma_{A,xx} + \sigma_{S,xx}$ can safely be approximated by $\sigma_{E,xx} \approx \sigma_{A,xx}$.

This extinction cross section is measured by allowing the focused fields of the two incident pulses to interact with the nanorod in the focal plane. Each of these pulses then induces a time-varying dipole moment in the nanorod. Given that only the longitudinal dipole resonance of the rod is of importance here, the dipole moment is oriented along the long axis (taken as the x-direction) and is given as the time-domain convolution between the x-component of the incident field at the nanorod position and the xx-component of the nanorod polarizability tensor. The field that is scattered by the nanorod into the far field is collected by the objective O2, together with the transmitted laser field, and detected by a photodiode PD. Again, the obscuration of O2 limits the minimum and maximum polar acceptance angles of the light rays that are collected. The detected power at time delay τ is given by $P(\tau) \sim \left\langle \left|\mathbf{E}(\theta,\phi,t,\tau)\right|^2 \right\rangle_{\theta,\phi,t} = 2P_0 + 2C(\tau)$. Here, the integration over the area of the second objective and the response time of the photodiode is abbreviated by $\langle\ \rangle_{\theta,\phi,t}$. The detected power contains a constant term P_0, which denotes the power of a single pulse, and a time delay-dependent correlation function $C(\tau) = \mathrm{Re}\left\langle \mathbf{E}(\theta,\phi,t)\cdot\mathbf{E}^*(\theta,\phi,t+\tau)\right\rangle_{\theta,\phi,t}$. From this field autocorrelation function (FAC) we can retrieve the frequency-dependent power spectrum $S(\omega)$ by calculating its Fourier transform $S(\omega) = \int_{-\infty}^{\infty} C(\tau)e^{i\omega t}d\tau$ [52]. If no particle is present in the focal spot only the directly transmitted pair of fields

$$\mathbf{E}(\theta,\phi,t,\tau) = \mathbf{E}_t(\theta,\phi,t) + \mathbf{E}_t(\theta,\phi,t+\tau) \quad (3)$$

is measured, apart from a scattering contribution from the substrate. However, by moving the nanorod into the focus, the nanoparticle generates a pair of scattered fields $\mathbf{E}_s(\theta,\phi,\mathbf{r}_0,t) + \mathbf{E}_s(\theta,\phi,\mathbf{r}_0,t+\tau)$ propagating in direction (θ,ϕ) towards O2. The scattered fields are given as

$$\mathbf{E}_s(\theta,\phi,\mathbf{r}_0,t) = \frac{1}{2\pi}\int_{-\infty}^{\infty} k^2\ddot{\mathbf{G}}_{FF}(\theta,\phi,\mathbf{r}_0,\omega)\alpha_{xx}(\omega)\tilde{\mathbf{E}}(\mathbf{r}_0,\omega)e^{-i\omega t}d\omega \quad (4)$$

beside a scattering contribution from the substrate. Here, $\ddot{\mathbf{G}}_{FF}(\theta,\phi,\mathbf{r}_0,\omega)$ denotes the far-field Green's tensor, $\alpha_{xx}(\omega)$ denotes the polarizability tensor component and $\tilde{\mathbf{E}}(\mathbf{r}_0,\omega)$ the frequency-dependent focal field at the position of the center of the nanorod $\mathbf{r}_0$. Thus, other than for the transmitted fields, the scattered field additionally depends on the position $\mathbf{r}_0$ of the nanorod in the focal plane.

The power detected by the photodiode is now given by the superposition of four fields, i.e. the directly transmitted field $\mathbf{E}_t$, the scattered field $\mathbf{E}_s$ from the nanorod and their time-shifted replicas. This is depicted in Figure 2A where a pair of ultra-broadband pulses excites a single nanorod inside the focal spot. As indicated in the image, the scattered fields now persist for longer times compared with the broadband exciting pulses due to the convolution of the incident field with the finite time-domain response function of the nanorod. The detected optical power at the photodiode can now be written as

$$P(\tau) = P_t(\tau) + P_s(\mathbf{r}_0,\tau) + P_{st}(\mathbf{r}_0,\tau). \quad (5)$$

This is a superposition of the directly transmitted power $P_t(\tau)$, the power $P_s(\mathbf{r}_0,\tau)$, which is scattered from the nanorod and the power $P_{st}(\mathbf{r}_0,\tau)$ resulting from the interference of the scattered and the transmitted fields. The scattered and the interference terms contain the desired information about the scattering and absorption cross section of the nanoparticle (Supporting Information S5).

Given that the extinction cross section of the nanorod is much smaller than the area of the laser focus spot, the detected power generated by the directly transmitted fields is much larger than from the scattered fields of the nanorod. Hence, the detected power $P(\tau) \approx P_t(\tau)$ is largely given by the transmitted field, which makes it difficult to retrieve the weak signal from the nanorod. This can be overcome by introducing a periodic modulation of the nanorods position in the confocal plane of the objectives [35, 53]. The amplitude of the scattered field, hence, the power $P_s(\mathbf{r}_0,\tau)$ and $P_{st}(\mathbf{r}_0,\tau)$, changes periodically when the nanorod is moved through the focal spot. Now, detecting the transmitted power $P(\tau)$ using a phase-sensitive lock-in amplifier and demodulation at the first ($1f$) or second harmonic ($2f$) of the modulation frequency results in $P_{1f/2f}(\mathbf{r}_0,\tau) \propto P_{sf}(\mathbf{r}_0,\tau) + P_{st}(\mathbf{r}_0,\tau)$, where the contribution of

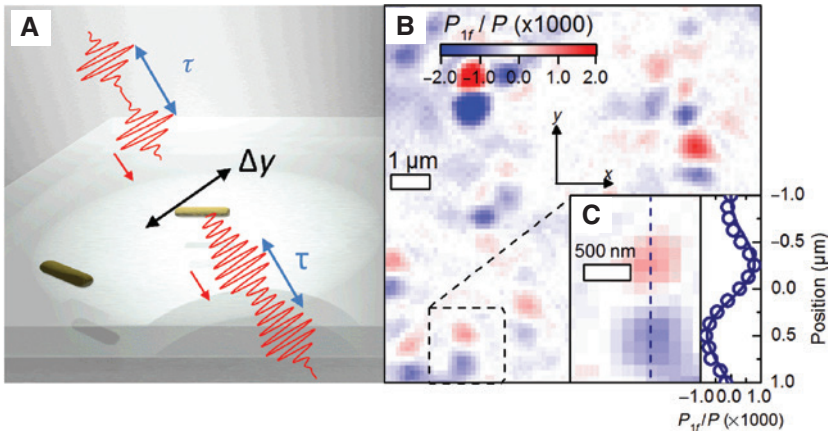

Figure 2: Schematic of the FT-SMS set-up and 2D map of the experiment.
(A) A phase-locked pair of linearly polarized ultra-broadband pulses, separated by a time delay τ, is focused onto the surface of a glass substrate that is covered with single gold nanorods. The position of the nanorods is periodically modulated in the *y*-direction and the transmitted and scattered light is collected in the far field. (B) The normalized map of P_{1f}/P recorded while scanning the nanorod sample through the laser focus. The power P_{1f} is retrieved by demodulating the transmitted power P at the modulation frequency 1*f*. The light scattering from a single nanorod appears as a dipolar pattern with positive and negative values of P_{1f}/P, oriented along the modulation axis y. Inset: The magnified map of a single nanorod. (C) Cross section (circles) taken along the dashed line in the inset. The solid line shows the expected line shape, given as the derivative of the Bessel-like intensity distribution of the focus.

the directly transmitted power is suppressed and only the terms containing the scattered fields remain.

In addition, the measured power at the photodiode in a real experiment suffers from high-frequency noise of the supercontinuum source as well as the read-out electronics [54]. This noise is independent of *f* so it can be additionally filtered out using the lock-in amplifier.

Now, the sample is raster-scanned along the *x*- and *y*-directions through the focal plane while modulating the nanorod position along the *y*-direction. The unmodulated signal $P(\tau)$ and the demodulated signals at the first and second harmonic are recorded simultaneously. In Figure 2B, a prototypical scan of the sample is depicted. It shows the demodulated power P_{1f} at time delays $\tau > 100$ fs, normalized to the transmitted power. These delays are significantly larger than the dephasing time of the nanorod (~16 fs) and the coherence time of the white-light source of less than 1 fs. The power P is directly recorded from the photodiode and is referred to as DC signal. Here, P_{1f}/P can become positive or negative, the sign describes the increase or decrease of the power modulation when moving the nanorod in or out of the focus spot. The areas of positive and negative values are adjacent along the modulation direction, whereas the nanoparticle is located at the node between these areas at $P_{1f}/P = 0$ [33]. The shape of the demodulated power for different positions of the sample $\mathbf{r}_0$ is given by the shape of the focal spot as well as the amplitude of the modulation. Within the limit of small modulation amplitudes, it can be approximated by the first (1*f*) or second derivative (2*f*) of the focal intensity with respect to the modulation axis (Supporting Information S6). This is depicted by the cross section in Figure 2C, which has been taken along the dashed line in the inset of Figure 2B. The blue circles represent the measured data, whereas the blue solid line is the characteristic line shape, which is calculated from the derivative of the Bessel-like intensity distribution of the incident beam [35]. The spatial separation between the minimum and the maximum is about 750 nm and yields the spatial resolution of the experimental set-up. This resolution is limited by the finite numerical aperture and obscuration of the used AROs. Significant improvements in both spatial resolution and signal-to-noise ratio can be achieved by replacing the AROs with glass objective, at the expense, however, of introducing significant chirp [48]. While most of the dipolar patterns in Figure 2C have a rather similar power ratio P_{1f}/P, some patterns, e.g. in the upper right corner, are more intense than others. We attribute these patterns to the agglomeration of multiple nanorods that are so close they become unresolvable in our experimental approach.

In order to extract the frequency-dependent extinction cross section of the particle, we measure the power P and P_{1f} at the positions of the maximum demodulated signal amplitude. The time delay τ of the excitation pulse pair is changed around their temporal overlap from –133 fs to +133 fs with a time increment of 266 as. The time increment Δt is chosen to be sufficiently small to be able to detect photon energies higher than the upper Nyquist limit of the FT measurements, $E_N = h/(2\Delta t) = 7.8$ eV, which

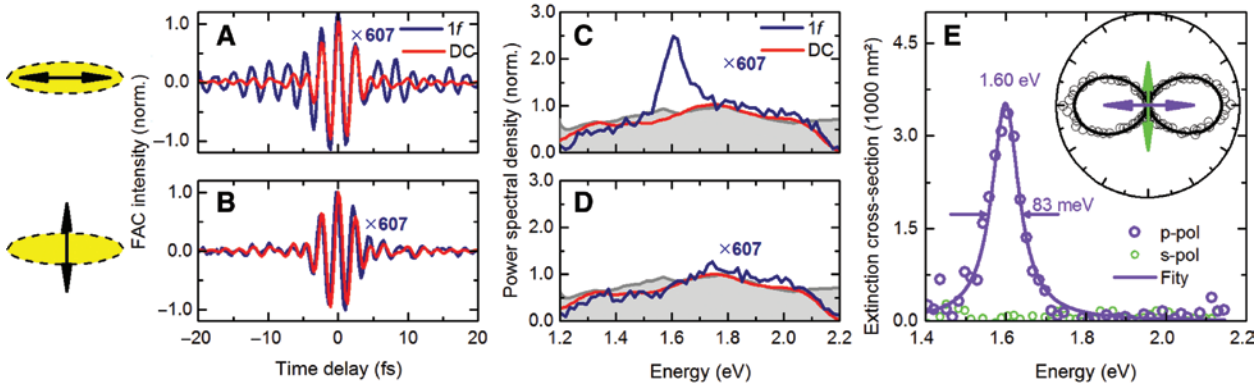

Figure 3: Experimental result of the FT-SMS measurement of a single gold nanorod.
(A + B) Field autocorrelation functions of the measured power ΔP (red solid line) and the demodulated power ΔP_{1f} (blue solid line) for incident polarization (A) parallel (p-pol) and (B) perpendicular (s-pol) to the longitudinal axis of the rod. (C + D) The power spectral densities of the field autocorrelation functions in (A) and (B). The laser spectrum is shown as a grey area. The corresponding normalization factors between the demodulated and the DC component are given. The peak at 1.60 eV in (C) is caused by the longitudinal SP resonance of the nanorod. (E) The background-corrected experimental extinction cross sections (circles) and Lorentzian fit (solid lines) for parallel (violet) and perpendicular (green) polarizations. Inset: The polarization dependence of the extinction cross section (open circles) and a $\cos^2$-fit (solid line).

is well above the highest photon energy of 3 eV delivered by the white light source. The power from the photodiode P and the demodulated power from the lock-in amplifier output P_{1f} are recorded simultaneously for each time delay. Since only the correlation function $C(\tau)$, i.e. the FAC function, contains the desired spectral information, ΔP and ΔP_{1f} are obtained by subtracting a constant offset $2P_0$ from the DC signal $P(\tau)$, i.e. $\Delta P = 2C(\tau) = P(\tau) - 2P_{0,DC}$ and from the demodulated power P_{1f}, i.e. $\Delta P_{1f} = 2C(\tau) = P_{1f}(\tau) - 2P_{0,1f}$. The constant offset is determined by averaging the measured power at long time delays τ. In Figures 3A and B, the normalized DC signal ΔP (red solid line) and the demodulated signal ΔP_{1f} (blue solid line) are shown for light polarized (A) along and (B) perpendicular to the longitudinal axis of the nanorod. The demodulated signal ΔP_{1f} is multiplied by a factor of 607 to reach the same scale as the DC signal ΔP. Both signals reveal a coherent modulation around the temporal overlap for light polarized along the transverse axis. Here, we determine an oscillation period of 2.4 fs, corresponding to the center wavelength of the laser source of 720 nm. The full width at half maximum (FWHM) of this FAC function is proportional to the inverse of the FWHM of the corresponding intensity spectrum of the laser source. When setting the excitation polarization parallel to the longitudinal axis of the nanorod, the oscillation period amounts to 2.4 fs around zero delay for both signals. However, in addition, a persistent additional oscillation for longer time delays is measured with a period of 2.6 fs only for the demodulated signal [55, 56]. The decay of the second oscillation reflects the plasmon dephasing time T_2 of the nanorod [57].

Now, the Fourier transform of the FAC traces for the DC and the 1*f*-component give the power spectral densities $S(\omega) = |\mathrm{FFT}(\Delta P(\tau))|$ and $S_{1f}(\omega) = |\mathrm{FFT}(\Delta P_{1f}(\tau))|$, respectively. Figures 3C and D depict the power spectral densities $S(\omega)$ (red solid line) and $S_{1f}(\omega)$ (blue solid line) for the excitation polarizations (C) that are parallel (p-pol) and (D) perpendicular (s-pol) to the longitudinal axis of the rod. For the perpendicular polarization, the power spectral densities of the DC and demodulated signals are similar to the incident laser spectrum (grey-shaded background), and differ only for higher (>2.1 eV) energies due to the filtering effects of optics in the beam path. Given that this background contribution is spectrally broad and follows the incident laser spectrum, we assign it to an off-resonant scattering contribution originating from the substrate. This may be reduced by optimizing the surface roughness of the substrate or by using higher NA objectives.

However, for the parallel polarization, the power spectral density of the demodulated signals contains a single narrowband peak at 1.6 eV on top of the broad spectrum from the laser source. This peak can be assigned to the longitudinal SP resonance of the nanorod. The peak amplitude directly yields the extinction cross section $\sigma_{E,xx}(\omega)$. As it is shown in more detail in the Supporting Information S5 and S6, the extinction cross section can be calculated as

$$\sigma_{E,xx}(\omega) \approx \sigma_{A,xx}(\omega) = \frac{A_F(\omega)}{b_1(\mathbf{r}_0,\omega)}\left(\frac{S_{1f}(\omega)}{S(\omega)}\right) - R(\omega), \qquad (6)$$

with $A_F(\omega)$ denoting the frequency-dependent focal area and $b_1(\mathbf{r}_0,\omega) = 0.55$ being a frequency-dependent Fourier

coefficient for the demodulation at 1*f*. In our analysis of the data, we subtract a polarization independent background $R(\omega)$, which can be assigned to the additional scattering of the underlying substrate and imperfect filtering by the lock-in amplifier. The resulting extinction spectrum of a single gold nanorod for the excitation directions that are parallel (violet circles) and perpendicular (green circles) to the nanorod long axis is shown in Figure 3E. To extract the quantitative results, the spectrum is fitted by a Lorentzian line shape function centered at 1.6 eV with a spectral width of $\Gamma = 83$ meV (FWHM) corresponding to a dephasing time $T_2 = 2\hbar/\Gamma$ of approximately 16 fs. This value matches the dephasing times of similar isolated particles in absence of inhomogeneous broadening, which have been deduced from previous studies [24, 29]. The magnitude of the extinction cross section reaches a value of 3500 nm², similar to results of other experimental and simulation studies [50]. The results of the polarization-resolved measurements are shown in the inset of Figure 3E. Here, the spectrally-integrated extinction cross section as a function of the polarization angle of the linearly polarized excitation is represented by open circles. The angle-dependent extinction cross section matches well a $\cos^2(\varphi)$ fit function (black solid line), with φ denoting the angle between the incident excitation polarization and the long axis of the nanorod [24]. This confirms that the data in Figure 3E indeed show the longitudinal SP resonance of a single particle. From the measured extinction spectrum for both polarizations, the SNR and the lower detection limit of our experimental approach can be estimated. While the signal is taken at the plasmon resonance of $\sigma_{ext} = 3500$ nm² when exciting the rod along the long axis, the noise level is determined by analyzing the spectra recorded by exciting the rod along the short axis. As shown in Chapter S8 of the Supplementary Information, we estimate a noise level of $\sigma_{noise} = 75$ nm². The $SNR = \sigma_{ext}/\sigma_{noise}$ is thus ~50, which is slightly below the SNR of 100 found in studies of rods with similar dimensions [58], and below the SNR of 1400 reported in [54]. Given that this main intention of the present experiments is to introduce a time-domain technique for SMS rather than to reach record SNR, we believe that the presented method is clearly competitive to more traditional CW methods. From the measured $\sigma_{noise} = 75$ nm², we estimate a lower detection limit of 150 nm² [54].

In our experiments, we did not attempt to precisely measure the geometry of each nanoparticle that has been studied spectroscopically. Scanning electron micrographs of several antennas reveal a variation of their longitudinal extension (average value $\langle d_x \rangle = 41$ nm with standard deviation $\sigma_x = 10$ nm) and transverse extension ($\langle d_y \rangle = 12$ nm, $\sigma_y = 3$ nm) axis size (Supporting Information S3). For comparison with the experiment, we thus performed FEM simulations to calculate the absorption for rods with different length d_x. The parameters of the simulations are depicted in Figure 4A. In the simulations, the rods are embedded in 1 nm thick polymer shell (refractive index 1.4) and placed on the surface of a planar substrate (BK7) with a refractive index of 1.51. The long axis of the rod is aligned along the *x*-axis and the linearly polarized laser field incident along the *z*-axis, which is perpendicular to the substrate. The height $d_y = 10$ nm and the width $d_z = 10$ nm of the rod are kept constant within the simulation, while d_x is varied. In Figure 4B, the calculated absorption cross

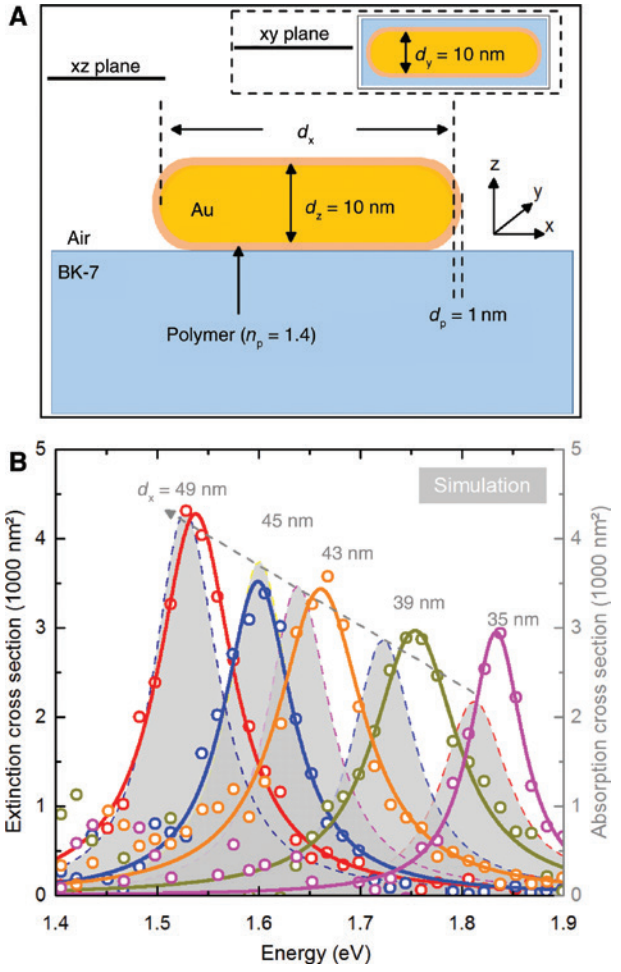

Figure 4: Comparison between experiment and FDTD calculations. (A) The sample geometry used in the FEM calculations. The gold rods are modeled as prolate spheroids with a longitudinal axis length d_x, a transverse axis length $d_y = 10$ nm and a height of $d_z = 10$ nm at an air-BK-7 interface. The rod is coated with a polymer shell of thickness of $d_p = 1$ nm with a refractive index of $n_p = 1.4$. (B) A comparison of the calculated absorption cross sections for different d_x shown as grey-shaded areas with respect to the experimentally measured extinction cross sections (circles) and their Lorentzian fits (solid lines).

sections for different rod lengths d_x are illustrated by gray-shaded areas. When decreasing d_x from 49 nm to 35 nm, the absorption cross section decreases from 4300 nm² for a 49-nm rod to 2200 nm² for a 35-nm rod and shows a significant spectral blueshift from 1.53 eV to 1.80 eV. The extinction cross sections from the single, isolated particles of varying length, which are measured using the FT-SMS set-up, are depicted by open circles in the same graph. The solid lines represent Lorentzian fits to the data. We find a good qualitative agreement between the experiment and simulation concerning both the spectral position and linewidth of SP resonance and the absolute values of the cross sections.

Indeed, the correlation between the red shift of the SP resonance and the decrease in extinction cross that is seen in the experiments and the simulations agree reasonably well. As we did not optically measure the exact lengths of each individual nanorod studied, we cannot claim that the observed trend in Figure 4 indeed reflects a length variation of the nanorods. Yet, we note that additional FEM simulations shown in Figure S4 of the Supporting Information reveal distinctly different correlations when varying the height, width or dielectric environment of the nanorod. This may suggest that length variations indeed play a dominant role for the variation of the optical properties of those nanorods. To analyze these correlations more precisely, measurements on particles with more precisely known geometries are currently underway.

A statistical analysis of the extinction cross section as a function of longitudinal SP resonance for 39 different, isolated nanorods is shown in Chapter S7 of the Supporting Information, together with the results from our numerical simulations and from a quasi-static model simulation [59]. From this, the accuracy in terms of the absolute extinction cross section of the experimental approach of ±1000 nm² can be estimated.

Finally, we demonstrate that the measured background $R(\omega)$ in the FT-SMS signals can be further decreased by detecting the scattered signal at the second harmonic of the modulation frequency. To this end, in Figures 5A and B, the maps of the transmitted relative power at (A) the fundamental modulation frequency P_{1f}/P and (B) twice the modulation frequency P_{2f}/P are shown. Both maps are normalized to their respective extrema and show two (1*f*), respectively, and three (2*f*) adjacent maxima and minima of the transmitted light at the position of each nanorod. The representative positions of a particle are indicated by the dashed ellipses in both graphs. As expected, the demodulated signals exhibit the characteristic shapes of the first and second derivatives of the focal intensity distribution along the modulation (*y*-) axis [33]. This is seen

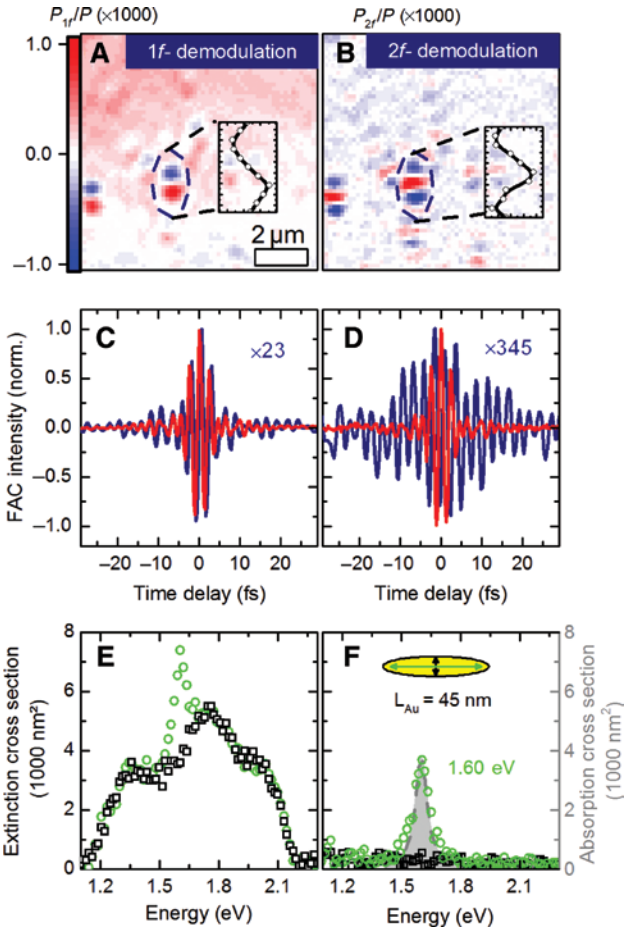

Figure 5: The demonstration of the background suppression using higher-order FT-SMS.
(A + B) The maps of the demodulated, normalized power P_{1f}/P and P_{2f}/P for demodulation frequencies of (A) 1*f* and (B) 2*f*. The position of the rod is marked by black ellipses in (A) and (B). The inset shows a cross section along the vertical axis of the black, dashed ellipse in each map. (C + D) Field autocorrelation functions of the transmitted light *P* (red solid line) and demodulated signals P_{1f} and P_{2f} (blue solid line) for excitation along the long axis of the rod. Normalization factors are indicated. (E + F) The extinction cross section of a single gold nanorod calculated from the field autocorrelation traces for light polarized along the long (green open circles) and the short axes (black open rectangles) at (E) 1*f* and (F) 2*f*. The extinction cross section in (F) is compared to the calculated absorption cross section of a nanorod with a long axis length of 45 nm.

in the cross section shown as insets. The map of P_{1f}/P in (A) exhibits a strong background signal in the upper part of the map reaching nearly the same magnitude as the positive value of the demodulated power induced by a nanoparticle. This enhanced background is seen in some samples and can be most probably attributed to a non-perfect cleaning procedure after the particle deposition process. However, as can be seen in (B), this background signal is strongly suppressed in the demodulated signal

at 2*f*, most probably due to a reduced cross-talk from the dominant DC component to the 2*f*- signal. Here, only the characteristic pattern of the second derivative of the Bessel-like intensity distribution along the *y*-axis is visible. This background suppression can be helpful in extracting single particle extinction spectra from the FAC traces as it is shown below.

In Figures 5C and D, field autocorrelation traces recorded for light polarized along the long rod axis are shown as blue solid lines for the demodulated signals (C) ΔP_{1f} and (D) ΔP_{2f}. For reasons of comparison, the normalized DC power ΔP is also depicted (red solid lines). The number in each plot denotes the normalization factors to reach the same scale as the DC signal. The signal at 2*f* consists of a rapidly decaying component at small time delays but carries an additional oscillation with a period around 2.4 fs that persists for more than 20 fs, whereas the signal at 1*f* almost exclusively shows the fast transient, similar to the DC signal. In Figures 5E and F, the extinction cross section deduced from these FAC traces are shown for the demodulated signal at (E) 1*f* and (F) at 2*f* for excitation polarizations parallel to the long axis (green open circles) and perpendicular to it (black open squares). For the parallel polarization, a single Lorentzian peak centered at 1.60 eV resides on a large energy-dependent background $R(\omega)$. This background is also visible for the light polarized perpendicular to the longitudinal rod axis and makes a quantitative analysis of the SP resonance difficult. In contrast, for the demodulation at 2*f*, this background nearly vanishes for both the s- and p-polarized light. The extinction cross section in Figure 5F shows a plasmonic resonance at 1.60 eV, which matches reasonably well with the absorption cross section calculated for a gold nanorod with $L_p = 45$ nm. Thus, the higher order modulation FT-SMS can effectively suppress background scattering and enable access to the extinction spectra of single particles embedded in strongly scattering environments. As shown in the Supplementary Information section, the SNR can be further improved by ~40% when detecting at twice the modulation frequency.

3 Conclusions

In summary, we have introduced a sensitive coherent spectroscopy method to determine the absolute value of the extinction cross section from the prolate nanorods. This technique is based on a combination of SMS and coherent FT spectroscopy. In a first application, we have used this technique to quantitatively measure the extinction spectra of the single gold nanorods. The experimentally determined extinction cross section of 3500 nm^2 for the longitudinal SP resonance of a 41-nm long nanorod centered at 1.6 eV matches well the extinction spectrum predicted by FEM simulations. Using higher-order demodulation, the signal-to-background ratio of the single-particle measurements can be drastically enhanced, enabling measurements of the linear spectral signatures of the single gold nanorods with high accuracy. By using the all-reflective objective, our set-up can be easily used with few-cycle light pulses with a pulse duration that is much shorter than the dephasing time of plasmonic nanostructures. Hence, in future applications it may not only be used to probe linear light scattering spectra but also to study coherent ultrafast optical nonlinearities with high resolution in the time domain. Using few-cycle laser pulses as the exciting laser source, this approach offers interesting perspectives for time-resolved and nonlinear spectroscopy of hybrid nanoparticles and, in particular, for probing plasmon-exciton interaction and coherent energy exchange processes in individual nanostructures on ultrafast time scales.

4 Methods

4.1 FT-SMS

The FT-SMS set-up is depicted in Figure 1A. A supercontinuum light source delivered coherent broadband optical pulses with pulse duration of 5 ps at a repetition rate of 40 MHz and an average power of up to 4W. A dispersion-balanced Mach-Zehnder interferometer was used to generate a pair of time-delayed pulses with a maximum optical path difference in the interferometer of 200 µm or maximum time delay of 666 fs. The average power of the pulse-pair was a few tens of µW after focusing by the objective O1. The FAC traces were recorded over a time delay range of ±133 fs around the temporal overlap, with a step size of 260 as. Thus, the achievable spectral resolution was 8 nm or 15 meV in the visible to near-infrared spectral range. A waiting time of 30 ms–50 ms per time delay step for time constants of 3 ms–10 ms at the Lock-In led to a total measurement time of 30 s–60 s per FAC trace.

4.2 Sample preparation

Glass substrates (BK-7) were cleaned in ethanol in an ultrasonic bath for 5 min. The glass substrates were rinsed sequentially with ethanol and deionized water,

followed by drying in an argon stream. Finally, an UV tip cleaner was used to oxidize their surfaces by UV/O_3 for 20 min. (UV.TC.EU.003, Bioforce Nanoscience, Inc. Ames). A volume of 2 µl of a suspension of chemically synthesized and polymer-coated gold nanorods (NanoPartz, specified concentration of 1.88×10^{14} nanorods per ml) was diluted with 10 ml of dried ethanol by ultrasonification for 15 min in a closed poly(tetrafluorethylene) (PTFE) container. An aliquot of 1 ml of this suspension was diluted with 9 ml of dried ethanol and sonicated for another 15 min in a closed PTFE container. The hydroxylated glass slides were placed in the PTFE container with the second nanorod dispersion for 2 h, during which they were immobilized onto the substrate. The nanorod density strongly depends on the nanorod concentration and immersion time of the glass slides in the nanorod dispersion. The obtained nanorod density was about 0.1 μm^{-2} as counted from SEM images.

4.3 FEM simulation

COMSOL Multiphysics 4.4 (RF Module) was used for the 3D numerical finite element method simulations of the gold nanorods with different lengths. The gold nanorods with various lengths ($d_x = 33$ nm to 49 nm) and height/width of $d_y = d_z = 10$ nm were covered in a 1 nm thick polymer shell ($n = 1.4$). The gold nanorods were placed at the air side of an interface between a substrate (BK-7, $n = 1.51$) and air. The values for the dielectric function of gold were taken from Johnson and Christy [60]. The vector Helmholtz equation was solved for scattered fields $\mathbf{E}_{tot} = \mathbf{E}_{in} + \mathbf{E}_s$, with the excitation $\mathbf{E}_{in}$ as an x-polarized plane wave propagating at normal incidence (labelled z-direction) to the air/Au and air/BK7 interface. The computation cell size in the simulation was 200 nm × 200 nm × 400 nm, with a mesh size varying from 0.075 to 7.5 nm. The "Perfectly Matched Layer" boundary conditions were applied to the outer boundaries of the computational space to eliminate the back-reflection from the boundaries. To decrease the computational time, the simulations were run for a quarter of the structure. Therefore, the "Perfect Electric Conductor" and "Perfect Magnetic Conductor" conditions were applied for the additional y-z and x-z planes passing through the center of the computational domain.

Acknowledgments: We gratefully acknowledge the financial support given by the Deutsche Forschungsgemeinschaft (SPP1839 and SPP1840), the Korea Foundation for International Cooperation of Science and Technology (Global Research Laboratory Project, K20815000003), the German-Isreali Foundation (Grant no. 1256) and the Graduate Program Nanoenergy of the State of Lower Saxony. M. S. wishes to thank the BMBF for a personal research grant "Photonic Transistors" from the NanoMatFutur program.

Author contributions: H.K. and M.S. built the optical set-up and performed the experiments and the data analysis. J.W. and A.M. prepared the nanorod samples. V.S. performed the FEM calculations. C.L. initiated the experiment and performed the analytical modelling of the data together with H.K. and M.S. The manuscript was written through the contributions of all authors. All authors have given their approval of the final version of the manuscript.

Conflict of interest statement: The authors declare no competing financial interest.

References

[1] Maier SA. Localized surface plasmons in plasmonics: fundamentals and applications. Boston, MA, Springer US, 2007, 65–88.
[2] Moskovits M. Surface-enhanced spectroscopy. Rev Mod Phys 1985;57:783–826.
[3] Willets KA, Van Duyne RP. Localized surface plasmon resonance spectroscopy and sensing. Annu Rev Phys Chem 2007;58:267–97.
[4] Yu Y, Chang SS, Lee CL, Wang CRC. Gold nanorods: electrochemical synthesis and optical properties. J Phys Chem B 1997;101:6661–4.
[5] Lee KS, El-Sayed MA. Gold and silver nanoparticles in sensing and imaging: sensitivity of plasmon response to size, shape, and metal composition. J Phys Chem B 2006;110:19220–5.
[6] Zuloaga J, Prodan E, Nordlander P. Quantum plasmonics: optical properties and tunability of metallic nanorods. ACS Nano 2010;4:5269–76.
[7] Grady NK, Halas NJ, Nordlander P. Influence of dielectric function properties on the optical response of plasmon resonant metallic nanoparticles. Chem Phys Lett 2004;399:167–71.
[8] Kern J, Großmann S, Tarakina NV, et al. Atomic-scale confinement of resonant optical fields. Nano Lett 2012;12:5504–9.
[9] Chikkaraddy R, de Nijs B, Benz F, et al. Single-molecule strong coupling at room temperature in plasmonic nanocavities. Nature 2016;535:127–30.
[10] Wiederrecht GP, Wurtz GA, Bouhelier A. Ultrafast hybrid plasmonics. Chem Phys Lett 2008;461:171–9.
[11] Large N, Abb M, Aizpurua J, Muskens OL. Photoconductively loaded plasmonic nanoantenna as building block for ultracompact optical switches. Nano Lett 2010;10:1741–6.
[12] Zheng YB, Kiraly B, Weiss PS, Huang TJ. Molecular plasmonics for biology and nanomedicine. Nanomedicine 2012;7:751–70.

[13] van Dijk MA, Lippitz M, Orrit M. Detection of acoustic oscillations of single gold nanospheres by time-resolved interferometry. Phys Rev Lett 2005;95:267–406.
[14] Manjavacas A, Garcia de Abajo FJ, Nordlander P. Quantum plexcitonics: strongly interacting plasmons and excitons. Nano Lett 2011;11:2318–23.
[15] Zengin G, Johansson G, Johansson P, Antosiewicz TJ, Kall M, Shegai T. Approaching the strong coupling limit in single plasmonic nanorods interacting with J-aggregates. Sci Rep 2013;3:3074.
[16] Melnikau D, Esteban R, Savateeva D, et al. Rabi splitting in photoluminescence spectra of hybrid systems of gold nanorods and J-aggregates. J Phys Chem Lett 2016;7:354–62.
[17] Simon T, Melnikau D, Sánchez-Iglesias A, et al. Exploring the optical nonlinearities of plasmon-exciton hybrid resonances in coupled colloidal nanostructures. J Phys Chem C 2016;120:12226–33.
[18] Santhosh K, Bitton O, Chuntonov L, Haran G. Vacuum Rabi splitting in a plasmonic cavity at the single quantum emitter limit. Nat Commun 2016;7:11823.
[19] Schlather AE, Large N, Urban AS, Nordlander P, Halas NJ. Near-field mediated plexcitonic coupling and giant rabi splitting in individual metallic dimers. Nano Lett 2013;13:3281–6.
[20] Vasa P, Wang W, Pomraenke R, et al. Real-time observation of ultrafast Rabi oscillations between excitons and plasmons in metal nanostructures with J-aggregates. Nat Photon 2013;7:128–32.
[21] Vasa P, Wang W, Pomraenke R, et al. Optical stark effects in J-aggregate-metal hybrid nanostructures exhibiting a strong exciton-surface-plasmon-polariton interaction. Phys Rev Lett 2015;114:036802.
[22] Sherry LJ, Jin R, Mirkin CA, Schatz GC, Van Duyne RP. Localized surface plasmon resonance spectroscopy of single silver triangular nanoprisms. Nano Lett 2006;6:2060–5.
[23] Schultz S, Smith DR, Mock JJ, Schultz DA. Single-target molecule detection with nonbleaching multicolor optical immunolabels. Proc Natl Acad Sci 2000;97:996–1001.
[24] Sönnichsen C, Franzl T, Wilk T, et al. Drastic reduction of plasmon damping in gold nanorods. Phys Rev Lett 2002;88:077402.
[25] Liu N, Tang ML, Hentschel M, Giessen H, Alivisatos AP. Nanoantenna-enhanced gas sensing in a single tailored nanofocus. Nat Mater 2011;10:631–6.
[26] Boyer D, Tamarat P, Maali A, Lounis B, Orrit M. Photothermal imaging of nanometer-sized metal particles among scatterers. Science 2002;297:1160–3.
[27] Tcherniak A, Ha JW, Dominguez-Medina S, Slaughter LS, Link S. Probing a century old prediction one plasmonic particle at a time. Nano Lett 2010;101398–404.
[28] Gaiduk A, Yorulmaz M, Ruijgrok PV, Orrit M. Room-temperature detection of a single molecule's absorption by photothermal contrast. Science 2010;330:353–6.
[29] Sönnichsen C, Geier S, Hecker NE, et al. Spectroscopy of single metallic nanoparticles using total internal reflection microscopy. Appl Phys Lett 2000;77:2949–51.
[30] Aurélien C, Paolo M, Fabrice V, Natalia Del F. Linear and ultrafast nonlinear plasmonics of single nano-objects. J Phys Condens Matter 2017;29:123002.
[31] Sönnichsen C, Franzl T, Wilk T, von Plessen G, Feldmann J. Plasmon resonances in large noble-metal clusters. New J Phys 2002;4:93.
[32] Berciaud S, Cognet L, Blab GA, Lounis B. Photothermal heterodyne imaging of individual nonfluorescent nanoclusters and nanocrystals. Phys Rev Lett 2004;93:257402.
[33] Arbouet A, Christofilos D, Del Fatti N, et al. Direct measurement of the single-metal-cluster optical absorption. Phys Rev Lett 2004;93:127401.
[34] Muskens OL, Del Fatti N, Vallée F. Femtosecond response of a single metal nanoparticle. Nano Lett 2006;6:552–6.
[35] Billaud P, Marhaba S, Grillet N, et al. Absolute optical extinction measurements of single nano-objects by spatial modulation spectroscopy using a white lamp. Rev Sci Instrum 2010;81:043101.
[36] Husnik M, Linden S, Diehl R, Niegemann J, Busch K, Wegener M. Quantitative experimental determination of scattering and absorption cross-section spectra of individual optical metallic nanoantennas. Phys Rev Lett 2012;109:233902.
[37] Li Z, Mao W, Devadas MS, Hartland GV. Absorption spectroscopy of single optically trapped gold nanorods. Nano Lett 2015;15:7731–5.
[38] Muskens OL, Del Fatti N, Vallée F, Huntzinger JR, Billaud P, Broyer M. Single metal nanoparticle absorption spectroscopy and optical characterization. Appl Phys Lett 2006;88:063109.
[39] Muskens OL, Dimitris C, Natalia Del F, Vallée F. Optical response of a single noble metal nanoparticle. J Opt A: Pure Appl Opt 2006;8:S264.
[40] Payne L, Zoriniants G, Masia F, et al. Optical microspectroscopy of single metallic nanoparticles: quantitative extinction and transient resonant four-wave mixing. Faraday Discuss 2015;184:305–20.
[41] Muskens OL, Billaud P, Broyer M, Del Fatti N, Vallée F. Optical extinction spectrum of a single metal nanoparticle: quantitative characterization of a particle and of its local environment. Phys Rev B 2008;78:205410.
[42] Muskens OL, Bachelier G, Fatti ND, et al. Quantitative absorption spectroscopy of a single gold nanorod. J Phys Chem C 2008;112:8917–21.
[43] Yorulmaz M, Hoggard A, Zhao H, et al. Absorption spectroscopy of an individual fano cluster. Nano Lett 2016;16:6497–503.
[44] Payne LM, Langbein W, Borri P. Polarization-resolved extinction and scattering cross-sections of individual gold nanoparticles measured by wide-field microscopy on a large ensemble. Appl Phys Lett 2013;102:131107.
[45] Vasa P, Pomraenke R, Cirmi G, et al. Ultrafast manipulation of strong coupling in metal – molecular aggregate hybrid nanostructures. ACS Nano 2010;4:7559–65.
[46] Savasta S, Saija R, Ridolfo A, Di Stefano O, Denti P, Borghese F. Nanopolaritons: vacuum Rabi splitting with a single quantum dot in the center of a dimer nanoantenna. ACS Nano 2010;4:6369–76.
[47] Fofang NT, Park TH, Neumann O, Mirin NA, Nordlander P, Halas NJ. Plexcitonic nanoparticles: plasmon-exciton coupling in nanoshell-J-aggregate complexes. Nano Lett 2008;8:3481–7.
[48] Piglosiewicz B, Sadiq D, Mascheck M, et al. Ultrasmall bullets of light-focusing few-cycle light pulses to the diffraction limit. Opt Express 2011;19:14451–63.
[49] Novotny L, Hecht B. Principles of nano-optics. Cambridge, Cambridge University Press, 2012.

[50] Davletshin YR, Lombardi A, Cardinal MF, et al. A quantitative study of the environmental effects on the optical response of gold nanorods. ACS Nano 2012;6:8183–93.
[51] Jain PK, Lee KS, El-Sayed IH, El-Sayed MA. Calculated absorption and scattering properties of gold nanoparticles of different size, shape, and composition: applications in biological imaging and biomedicine. J Phys Chem B 2006;110:7238–48.
[52] Born M, Wolf E, Bhatia AB, et al. Principles of optics: electromagnetic theory of propagation, interference and diffraction of light. Cambridge, UK, Cambridge University Press, 2000.
[53] Crut A, Maioli P, Del Fatti N, Vallee F. Optical absorption and scattering spectroscopies of single nano-objects. Chem Soc Rev 2014;43:3921–56.
[54] McDonald MP, Vietmeyer F, Aleksiuk D, Kuno M. Supercontinuum spatial modulation spectroscopy: Detection and noise limitations. Rev Sci Instrum 2013;84:113104.
[55] Petek H, Ogawa S. Femtosecond time-resolved two-photon photoemission studies of electron dynamics in metals. Prog Surf Sci 1997;56:239–310.
[56] Mårsell E, Losquin A, Svärd R, et al. Nanoscale imaging of local few-femtosecond near-field dynamics within a single plasmonic nanoantenna. Nano Lett 2015;15:6601–8.
[57] Lamprecht B, Krenn JR, Leitner A, Aussenegg FR. Particle-plasmon decay-time determination by measuring the optical near-field's autocorrelation: influence of inhomogeneous line broadening. Appl Phys B 1999;69:223–7.
[58] Devadas MS, Li Z, Hartland GV. Imaging and analysis of single optically trapped gold nanoparticles using spatial modulation spectroscopy. J Phys Chem Lett 2014;5:2910–5.
[59] Bohren CF, Huffman DR. Absorption and scattering by a sphere. In: Bohren CF and Huffman DR, eds. Absorption and scattering of light by small particles. Wiley-VCH Verlag GmbH, Weinheim, Germany, 2007, 82–129.
[60] Johnson PB, Christy RW. Optical constants of the noble metals. Phys Rev B 1972;6:4370–9.

Supplemental Material: The online version of this article offers supplementary material (https://doi.org/10.1515/nanoph-2017-0096).